Title

KSHV Topologically Associating Domains in Latent and Reactivated Viral Chromatin

Journal

Journal of Virology, 96(14)

ISSN

0022-538X

Authors

Campbell, Mel

Chantarasrivong, Chanikarn

Yanagihashi, Yuichi

et al.

Publication Date

2022-07-27

DOI

10.1128/jvi.00565-22

Peer reviewed

AMERICAN SOCIETY FOR MICROBIOLOGY | Journal of Virology®

GENOME REPLICATION AND REGULATION OF VIRAL GENE EXPRESSION

KSHV Topologically Associating Domains in Latent and Reactivated Viral Chromatin

Mel Campbell,[a] Chanikarn Chantarasrivong,[b] Yuichi Yanagihashi,[c] Tomoki Inagaki,[a] Ryan R. Davis,[d] Kazushi Nakano,[b] Ashish Kumar,[a] Clifford G. Tepper,[e,f] Yoshihiro Izumiya[a,e,f]

[a]Department of Dermatology, School of Medicine, University of California Davis (UC Davis), Sacramento, California, USA
[b]Lifescience Division, Lifematics, Osaka, Japan
[c]Biological Data-Science Division, Lifematics, Osaka, Japan
[d]Department of Pathology and Laboratory Medicine, School of Medicine, UC Davis, Sacramento, California, USA
[e]Department of Biochemistry and Molecular Medicine, School of Medicine, UC Davis, Sacramento, California, USA
[f]UC Davis Comprehensive Cancer Center, Sacramento, California, USA

Mel Campbell and Chanikarn Chantarasrivong contributed equally to this article. Author order was determined by discussion and agreement among all authors.

ABSTRACT Eukaryotic genomes are structurally organized via the formation of multiple loops that create gene expression regulatory units called topologically associating domains (TADs). Here we revealed the KSHV TAD structure at 500 bp resolution and constructed a 3D KSHV genomic structural model with 2 kb binning. The latent KSHV genome formed very similar genomic architectures in three different naturally infected PEL cell lines and in an experimentally infected epithelial cell line. The majority of the TAD boundaries were occupied by structural maintenance of chromosomes (SMC1) cohesin complex and CCCTC-binding factor (CTCF), and the KSHV transactivator was recruited to those sites during reactivation. Triggering KSHV gene expression decreased prewired genomic loops within the regulatory unit, while contacts extending outside of regulatory borders increased, leading to formation of a larger regulatory unit with a shift from repressive to active compartments (B to A). The 3D genomic structural model proposes that the immediate early promoter region is localized on the periphery of the 3D viral genome during latency, while highly inducible noncoding RNA regions moved toward the inner space of the structure, resembling the configuration of a "bird cage" during reactivation. The compartment-like properties of viral episomal chromatin structure and its reorganization during the transition from latency may help facilitate viral gene transcription.

IMPORTANCE The 3D architecture of chromatin allows for efficient arrangement, expression, and replication of genetic material. The genomes of all organisms studied to date have been found to be organized through some form of tiered domain structures. However, the architectural framework of the genomes of large double-stranded DNA viruses such as the herpesvirus family has not been reported. Prior studies with Kaposi's sarcoma-associated herpesvirus (KSHV) have indicated that the viral chromatin shares many biological properties exhibited by the host cell genome, essentially behaving as a mini human chromosome. Thus, we hypothesized that the KSHV genome may be organized in a similar manner. In this report, we describe the domain structure of the latent and lytic KSHV genome at 500 bp resolution and present a 3D genomic structural model for KSHV under each condition. These results add new insights into the complex regulation of the viral life cycle.

KEYWORDS CTCF, Capture Hi-C, epigenetics, KSHV, ORF50, TAD, genome organization, transcriptional regulation

Editor Jae U. Jung, Lerner Research Institute, Cleveland Clinic

Address correspondence to Yoshihiro Izumiya, yizumiya@ucdavis.edu.

The authors declare no conflict of interest.

Received 5 April 2022
Accepted 21 June 2022
Published 11 July 2022

Kaposi's sarcoma-associated herpesvirus (KSHV), also known as human herpesvirus-8 (HHV8), is a member of the gammaherpesvirus family of double-stranded DNA viruses. The virus is strongly associated with Kaposi's sarcoma (KS), an endothelial cell-derived tumor, and two rare lymphoproliferative disorders, multicentric Castleman's disease (MCD) and primary effusion lymphoma (PEL). KSHV exhibits a broad host range and can infect a variety of cell types *in vitro*, including B lymphocytic cells, renal-derived cells, and human gingival epithelial cells (1–3). KSHV DNA exists in the virion as a linear duplex of ~140 kb of coding sequence which encodes approximately 80 genes or open reading frames (ORFs) that are expressed in a highly coordinated manner during latency or lytic replication (4, 5). The viral coding sequences are flanked on either side by tandem terminal repeats of highly GC-rich noncoding sequences, giving rise to a genome of ~160–170 kb (6, 7). Following infection, the chromatin-free viral genome circularizes, is rapidly chromatinized (8), then maintained and replicated in the nucleus of the host cell as monomeric episomes. A crucial element of the KSHV life cycle is the reactivation of the virus from a latent (dormant) state into the lytic replicative cycle in which viral genomic DNA is replicated, viral particles are produced, then virions released along with host cell lysis.

A great deal of effort has focused on defining the epigenetic mechanisms that regulate latency, reactivation, and commandeering of the host cell by KSHV (9–11). Although a single viral protein, K-Rta (ORF50), triggers the onset of lytic replication by the transcriptional activation of lytic genes, the exact details of how K-Rta functions as this master regulator have been enigmatic. We have previously shown that interplay between KSHV-encoded transcription factors and host cell-encoded epigenetic regulators (JMJD2A demethylase, EZH2 methyltransferase) are key mechanisms in controlling KSHV reactivation (8, 12). In addition, using Capture Hi-C (chromosome conformation capture analyses with deep sequencing) analyses of the KSHV genome, we demonstrated that K-Rta not only activates individual lytic genes by binding to specific regulatory elements along the KSHV genome, but that it also performs a higher-order coordination of the process by mediating three-dimensional (3D) conformational changes in the architecture of the KSHV chromosome (13). In essence, "chromatin loops" are formed via K-Rta promoting contact between distant genomic regions containing key regulatory sequences.

Advances in chromosome conformation capture (3C)-based studies have uncovered the existence of spatially insulated genomic regions that are now considered the invariant building blocks of chromosomes (14–17). When initially reported in 2012, these ~100 kb to1 Mb regions were referred to as topological domains (14) or topologically associating domains (TADs) (15). These domains are defined by the preferential interaction of loci located within a given TAD and a relative (~2-fold) depletion of interactions between loci located in different TADs (16). In the era of 3C-based methods, TADs were originally described in mammalian cells (14, 15) using high-throughput chromosome conformation capture (Hi-C) (18) or chromosome conformation capture carbon-copy (5C) (19), and in Drosophila (17) chromosomes using Hi-C. However, TADs have also been found in Zebrafish (20), *Caenorhabditis elegans* (21), *Saccharomyces cerevisiae* (22) and *Schizosaccharomyces pombe* (23). In addition, analysis of nucleoids of *Caulobacter crescentus* (24) and *Bacillus subtilis* (25, 26) have described genomic spatial domains termed Chromosomal Interaction Domains (CIDs), which mimic TADs in terms of preferential interaction properties. Together, these results suggest that TAD-like domains, although differing in size among the genomes of the various species analyzed (27), may be a universal feature of both prokaryotic and eukaryotic genomes.

The existence of TAD-like structures within the genomes of large double-stranded DNA viruses such as herpesvirus family has not been reported. For KSHV there are numerous reports concerning the role of the structural maintenance of chromosomes (SMC) cohesin complex and CCCTC-binding factor (CTCF) in control of viral latency and reactivation (28–36). As both cohesin and CTCF have been linked to chromatin looping formation in mammalian cells (14, 37–39), this suggests the plausible existence of TAD-

like structures within KSHV genomes. Moreover, previous 3C (33) and capture Hi-C (13) analyses have documented the presence of chromatin looping within the latent and lytic KSHV genomic regions. Together with KSHV epigenomic mapping data (8, 12, 40–43), this suggests that the chromatinized KSHV genome shares many biological properties exhibited by the host genome, behaving as a mini human chromosome and, as such, may be organized in a TAD-like manner. In this report, we describe the TAD-like structures of the latent and lytic KSHV genome at 500 bp (bp) resolution and present a 3D genomic structure model for the KSHV under each condition.

RESULTS

KSHV topologically associating domains. In our previous study, we demonstrated that the KSHV genome forms organized DNA loops in infected cell nuclei and the frequency of these loops increased during reactivation, especially near K-Rta binding sites (13, 44). In order to understand the molecular details of loop formation, we have performed additional Capture Hi-C experiments to augment the results from our earlier publication. Previously, our experimental workflow utilized an in-house 3C procedure based on Gavrilov et al. (45) with a single restriction enzyme digestion prior to library capture with KSHV lockdown probes (13). In the current study, a commercially available Hi-C kit (Arima Genomics) was used in conjunction with our probe library. In this procedure, the chromatin digestion step is performed *in situ* and employs a restriction enzyme cocktail coupled with fill-in reactions to incorporate a biotinylated deoxynucleotide to mark the digested ends, which facilitates the enrichment of the DNA ligation products (i.e., consisting of the spatially proximal digested ends) prior to the KSHV lockdown probe capture step (Fig. 1A and Fig. S1A). The restriction enzyme digestion generated fragment sizes with an average length of 190 bp $\pm$ 210 bp. The largest fragment is 2,225 bp, which is located near the LANA coding region, while the shortest fragment is 4 bp. The distribution of fragment sizes is shown in Fig. S1B. A total of 3,565,321 valid read pairs were uniquely mapped on the KSHV genome in nonreactivated BCBL-1 cells, while 5,967,349 valid read pairs were mapped in the reactivated sample. Using two capture/enrichment steps, we further increased the number of sequence reads corresponding to valid Hi-C di-tags by approximately 1,000-fold over our previous studies and prepared KSHV genomic interaction maps at 500 bp resolution (Fig. 1B–D).

The diagram in Fig. 1B provides explanation of the resulting heat maps, which visualize the Hi-C contact matrix of the entire KSHV genome and reveal TADs. Because TADs often refer to sizes of 100 kb to 1 Mb genomic domains (14), we decided to use the term of transcription regulatory domain (TRD). The regions surrounded by red triangles are identified as TRDs, which demonstrate frequent genomic loops within the genomic regions. The color scale corresponded to the frequency of the genomic contacts compared to that of theoretical interactions; a higher frequency of interactions over theoretically predicted ones based on linear distance is depicted as darker red color, while blue indicated lower than theoretically-expected frequencies of genomic interactions detected with linear distance. Because our analysis was based on calculations assuming linear chromosomes while the KSHV genome is circular, distant genomic regions tends to be identified with a greater frequency of genomic contacts than theoretically calculated. Therefore, we focused on genomic contacts formed in more proximal regions (e.g., $<$50 kb) in this analysis. Each contact represents a KSHV-KSHV read pair and the map displays as a contact matrix visualized as a heat map with subdivision of the KSHV genome into a bin size of 500 bp. The results showed that three naturally infected PEL cell lines (TREx-BCBL-1, BC1 and BC3) exhibited very similar TRD structures (Fig. 1C). For the K-Rta inducible TREx-BCBL-1 cell line, we performed biological triplicate analyses to assess experimental variation.

In addition to naturally infected B-cell lines, we also determined the KSHV TRD structure in experimentally infected iSLK/Bac16 cells to assess cell type dependence (Fig. 1D). The results demonstrated very similar TRD structures to those of the naturally

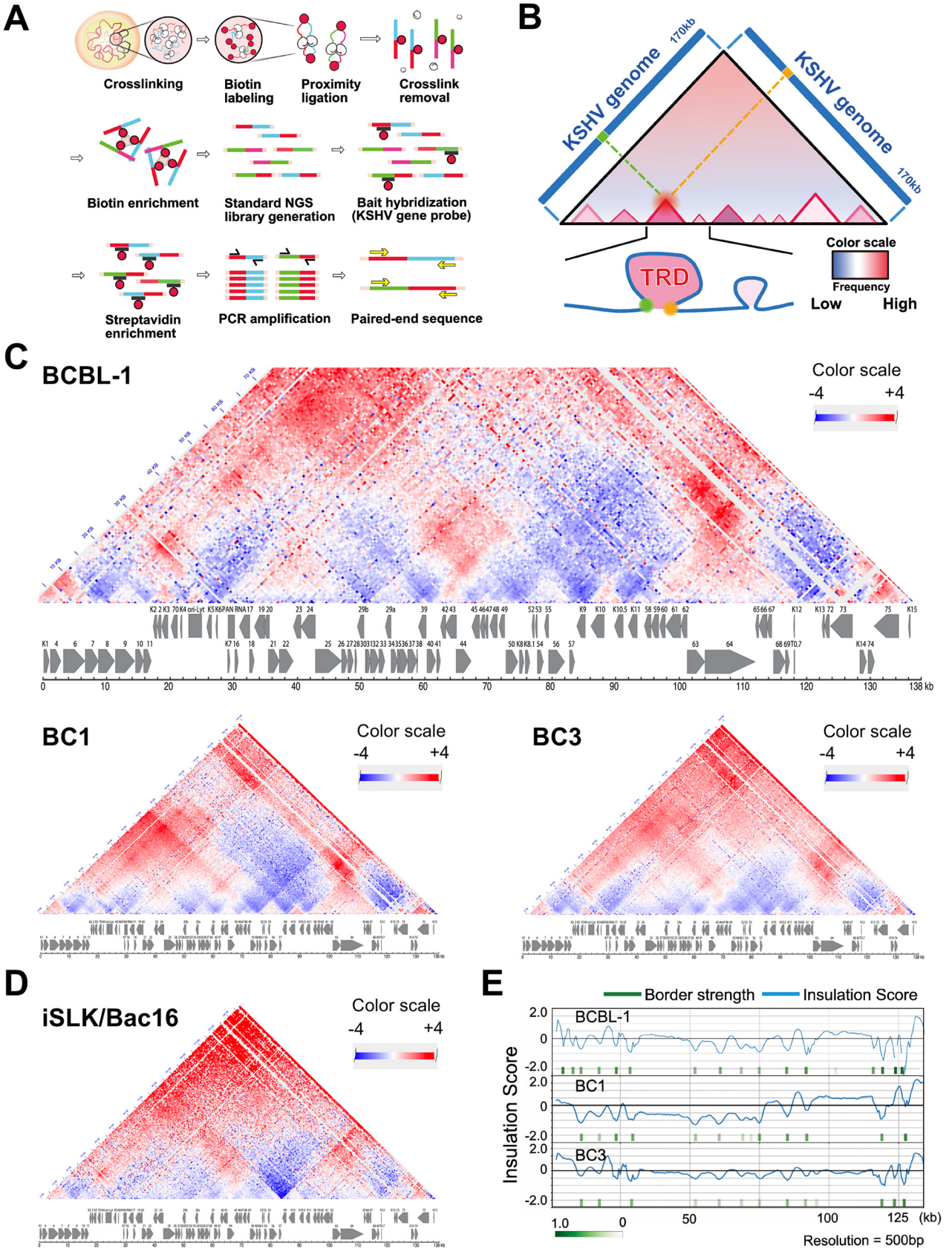

FIG 1 KSHV genomic contact map. (A) Capture Hi-C procedure. Biotin-labeled nucleotide and biotin-labeled tiling oligos are used to enrich successfully ligated and KSHV genome-containing DNA fragments. (B) Representative Hi-C contact map. Diagram of representative Hi-C contact

(Continued on next page)

infected cells. Our TRD map also agreed with previous 3C studies that positioned the LANA promoter region forming genomic loops with K12 loci at higher frequencies (31). The position of borders for the genomic domains were also identified mathematically (Fig. 1E). Although the results showed a similarity in genomic domain structure among three PEL cell lines, when we directly compared relative frequencies of sequence reads from individual domains among three PEL lines, each cell line displayed differences (Fig. S2). For example, BC1 showed more genomic loops at the K1–K8 region than BCBL-1, while BC3 maintained more genomic contacts at late gene cluster regions than BCBL-1.

Regulation of KSHV genomic domain formation. By overlaying histone modification and transcription factor binding sites, we next examined their association with TRD formation (Fig. 2A–C). Although the genomic domains are not defined by chromatin state, sites of histone modification aligned very well with TRD and were organized with genomic domains with active histone marks (H3K4me3, H3K27Ac). The genomic regions with active histone marks seem to be physically neighboring each other in the 3D structure, which is seen by higher frequencies of genomic ligations than the theoretically expected ligated sequence reads (shown in red, where two H3K4me3 marked genomic regions were ligated more frequently than theoretically expected frequency), and these features were common in all cell lines tested. The results also demonstrated that TRDs could also be distinctly separated based on the reactivation kinetics class of KSHV gene expression. For instance, late gene clusters were localized in distinct TRDs (within separated triangles), and the genomic regions appeared to be distantly located from other genomic regions or were too condensed to interact with open chromatin regions (IE and E clusters) and established a genomic domain essentially only within the late gene cluster in latent chromatin. In all cell lines tested, the latent gene cluster region (K13–ORF72) demonstrated frequent genomic loops with genomic regions encoding viral interferon regulatory factors (K9–K11) and also formed genomic domains with downstream genomic loci (ORF75–K15). Consistent with previous reports, CTCF localizes to the junctions of the majority of TRDs, and CTCF indeed colocalized with SMC1 on the KSHV genomes (Fig. 2B and C). In addition, superimposing K-Rta recruitment sites that were reported previously (46) further showed that K-Rta recruitment sites (Fig. 2C, black line) localized adjacent to CTCF/SMC1 binding sites (Fig. 2C, red and blue lines), and the genomic regions harbored poised/stalled RNAPII (Fig. 2C, shadow). The results indicate that the KSHV episome is structured to allow the K-Rta complex access to genomic hubs, which may serve to maximize K-Rta transactivation function. The next-generation sequencing (NGS) plot further confirmed that K-Rta binding sites are closely localized to CTCF and RNAPII binding sites (Fig. 2D).

Regulation of TAD structure during reactivation. Having defined the KSHV genomic TRD structure in the condition that the majority of episomes were in during the latent state, we next examined changes in TRDs induced during the early stages of reactivation. To avoid complications with ongoing DNA replication, we examined a time point (i.e., 24 h post-reactivation) at which there was an only minimal increase in viral DNA copies, as measured by qPCR (Fig. S3) (47). Capture Hi-C analyses were performed with TREx-BCBL-1 cells at 0 and 24 h post-reactivation using an induction protocol consisting of a combination of tetradecanoyl phorbol acetate (TPA) and doxycycline. The experiments were performed in triplicate. Using the TAD caller program TADbit for visualization of hierarchical genomic domains, the formation of larger TRDs during reactivation was observed when compared with TRD structures observed during latency, and presumably proceeded through the fusion of neighboring TRDs via assembly of active

FIG 1 Legend (Continued)
map is presented. (C) KSHV genome contact maps in both naturally infected cells (PEL cells, BCBL-1, BC1, and BC3) and (D) experimentally infected cells (iSLK/BAC16 cells). Genomic contacts detected at more than expected frequencies are depicted in red, while underrepresented contacts between loci are shown in blue. A color range scale is listed and KSHV ORF maps are shown beneath each contact map. (E) Position of transcription regulatory domain borders. Insulation scores and positions of borders are calculated based on direction of genomic loop and looping frequencies. Borders are indicated by green vertical rectangles and insulation score is shown by the continuous blue lines.

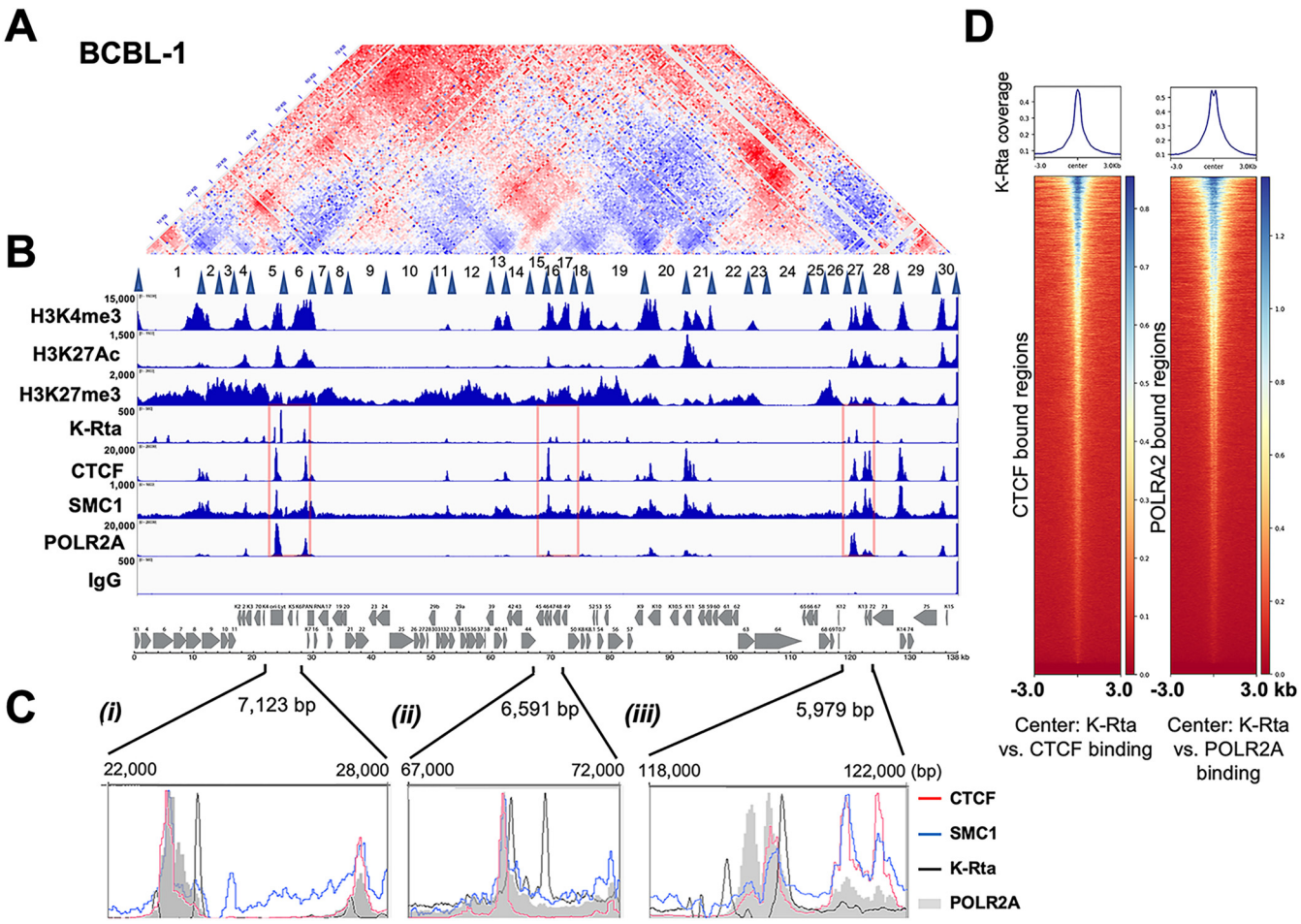

FIG 2 Superimposition of select histone modifications and protein factor binding sites on genomic contacts of the latent KSHV genome. (A) The BCBL-1 contact map. The BCBL-1 contact map from Fig. 1C is shown. Latent TRDs numbered 1–30 with their borders (blue triangles) (from Fig. 3A) are listed below the contact map. (B) Histone modification and protein recruitment sites. Alignment of histone modifications H3K4Me3, H3K27Ac, H3K27me3, and binding sites of K-Rta (TREx-BCBL-1; reactivated, 12 h), CTCF, SMC1, and POLR2A in BCBL-1 from CUT&RUN or ChIP-seq (K-Rta) are shown. Control IgG for background control with CUT&RUN is also shown. The sequence reads were mapped to the KSHV genome. IGV snapshots and a KSHV genome map are shown. Numbers on the left-hand side of each track denotes the height of the peak (e.g., read depth). (C) Zoomed view of CTCF, SMC1, K-Rta, and RNAPII enrichment at select regions of the KSHV genome (*i*) K4-PAN RNA, (*ii*) ORFs 45–50, and (*iii*) K12 region. (D) Genome-wide correlation among K-Rta, CTCF, and RNAPII recruitment sites. Density plots showing average K-Rta ChIP-seq signals within ±3 kb regions around the center of CTCF or POLR2A peaks. The heatmap shows K-Rta signals on CTCF or POLRA2 CUT&RUN peaks. The *y* axis is ranked according to CTCF or POLR2A enrichment in descending order.

transcription sites, (Fig. 3A) (44). The results also showed that preexisting genomic loops in latent cells (Fig. 2A, red) were largely disrupted during reactivation, as indicated by a marked decrease in the frequency of their interactions within individual TRDs (Fig. 3B, blue). While preexisting TRDs were decreased, genomic contacts that spanned outside of the previously existing TRD borders were increased (Fig. 3B, red). Reactivation was also characterized by new interactions of the K-Rta promoter region formed with the late gene clusters (ORF63–68), while preformed, latency-associated contacts with active compartments, such as E gene clusters (ORF6–ORF11) were decreased (Fig. 3B).

Next, insulation scores were calculated to reveal changes in TRDs before and after reactivation. A lower score suggests a higher insulation effect, which is indicative of the position of the boundary. The border strength at the majority of genomic regions was decreased in reactivating samples (Fig. 3C), suggesting genomic fragments more freely interacted with other genomic domain fragments when viral lytic gene expression was triggered. As expected, compartment analyses showed shifts from repressive to active compartments (B to A) during reactivation [Fig. 3D]. Interestingly, the analyses also showed that E gene clusters encompassing sequences from K1 to PAN RNA coding regions (genomic locations bin 1–60 [1–30 kb region]) showed an active compartment

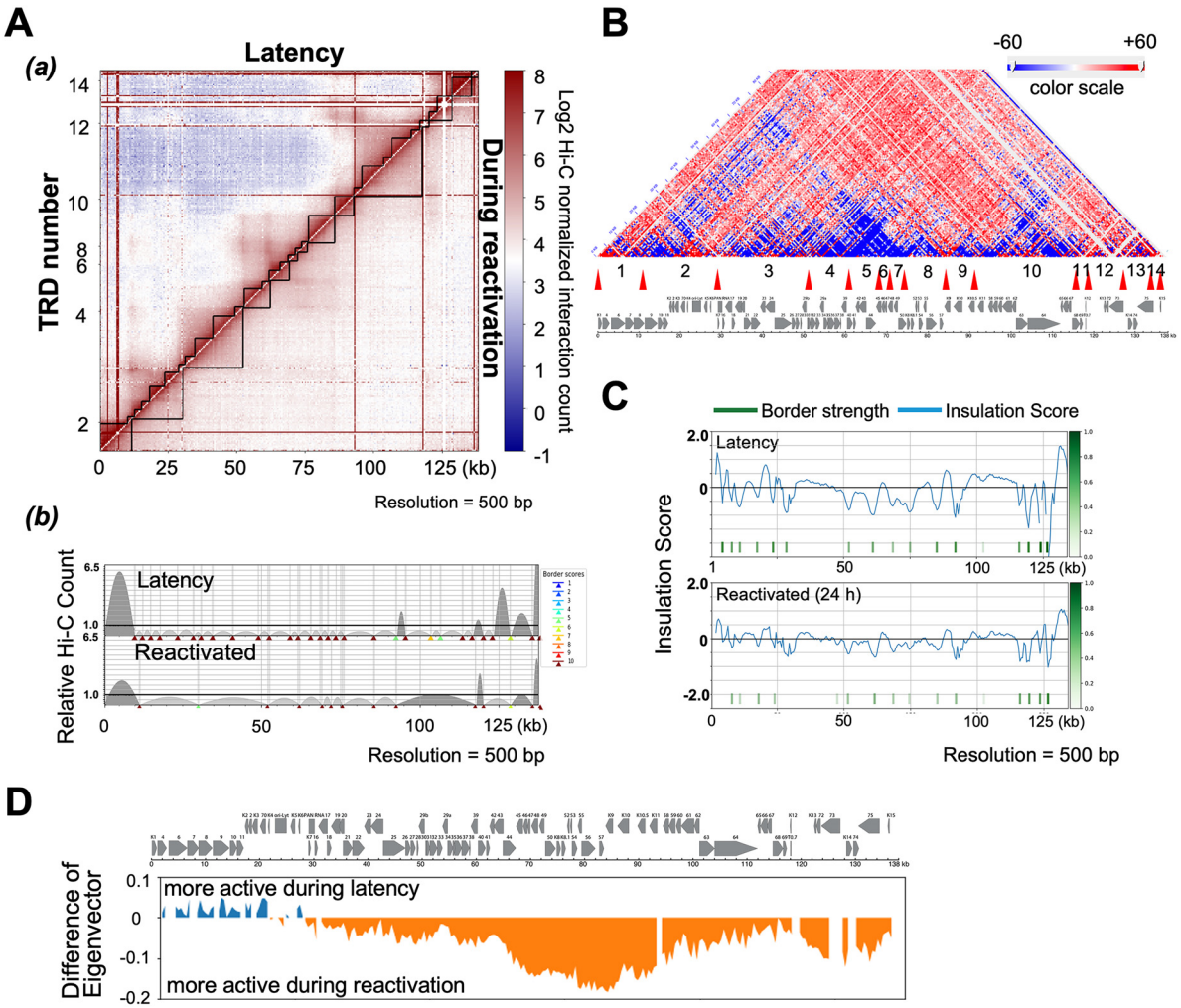

FIG 3 Dynamics of genomic contacts by reactivation. (A) Interaction frequency matrix. TRDs were calculated and visualized with TADbit, and genomic domains defined by frequencies of DNA contacts are marked with black solid lines along the diagonal (*a*). TAD border alignment during latency (upper) and during reactivation (lower) are shown (*b*). Dark and light gray arches indicate TRDs with higher and lower than expected intra-TRD interactions, respectively. TADbit border robustness (from 1–10) is identified by a color gradient from blue to red. (B) Contact heatmap: BCBL-1 reactivation versus latency. Contacts are color coded as described in Fig. 1 (red, increased contacts; blue decreased contacts). TRDs called during reactivation (Fig. 3A) numbered 1–14 with their borders (red triangles) are listed below the contact map. The KSHV ORF map is included in the bottom panel. The portion of figures (A and B) are adapted and modified from a previously published book chapter (44). (C) TAD border analyses. Insulation score (border strength) is plotted (*a*). Reactivation reduced insulation and border strength to create larger transcription units (*b*). (D) Compartment analysis. 500 bp bins were identified as in compartment A or B by calculating eigenvectors.

structure in latent chromatin. This result is somewhat unexpected since these genomic loci largely encode lytic genes. While LANA, two Ori-Lyts regions, K10.5/11, and the PAN RNA coding region did not change, a specific genomic compartmental structural shift occurs between latency and after triggering reactivation. These genomic regions are found to be narrowly insulated with higher CTCF/SMC1 peaks (Fig. 2B).

KSHV 3D genomic structure: a bird cage model. With 3,565,321 (latent) and 5,967,349 (lytic) valid Hi-C di-tags (i.e., genomic contacts) covering the ~140 kb KSHV genome, we next constructed a theoretical 3D KSHV genomic structural model utilizing TADbit, which was then visualized with the UCSF Chimera program (48). The model proposes that the immediate early promoter region (e.g., K-Rta) is localized on the periphery of the 3D viral genome during latency, which is likely to be more accessible to the nuclear environment (Fig. 4, Supplemental material movie); while the highly inducible long noncoding RNA region (i.e., PAN RNA) moved toward the inner space of the structure in reactivating episomes. During the transition from latency to the lytic cycle,

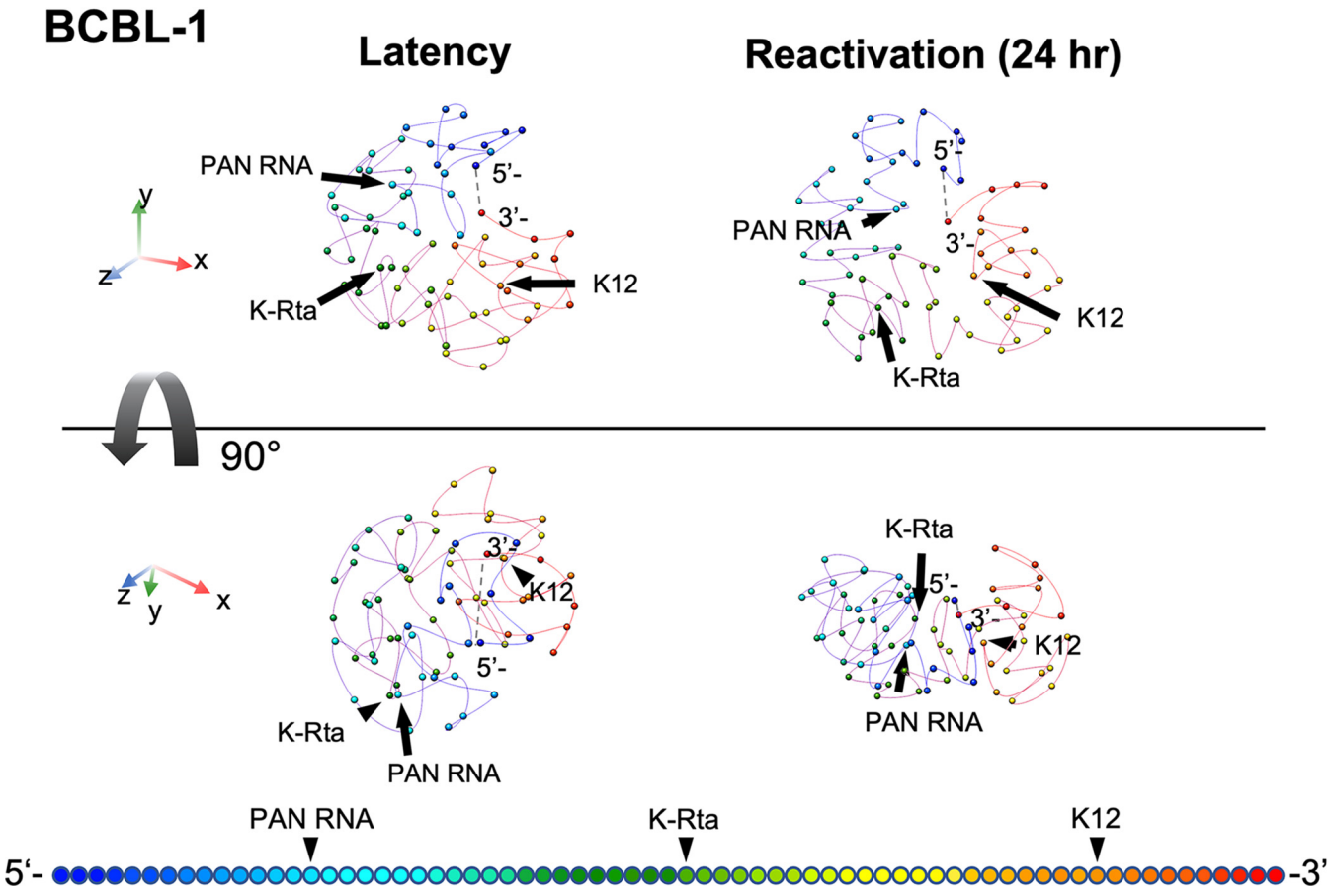

FIG 4 KSHV 3D genomic structure modeling. Frequencies of ligated fragments were used to calculate distances between fragments at 2 kb resolution. The average of 8 different models were used to draw the figures. KSHV 3D genomic structure before (left) and after (right) triggering reactivation are shown. The 90-degree rotated views are also shown in the panels (bottom). Color gradation associated with KSHV genomic position are depicted at the bottom of figures. The movies of the 3D figures including individual 8 models in shadow are presented in Fig. S5. The dotted line in each structure represents the putative terminal repeat (TR) position. Each sphere marks 2 kb of linear genomic sequence.

the overall 3D genomic structures were squeezed into a doughnut-like configuration from a spherical shape. This arrangement positions the transcriptionally active regions (i.e., PAN RNA, and K12) to be more closely neighboring to other genomic loci in three-dimensional space, and their conformation change approximates a "bird cage" (Fig. 4). These changes were also consistent with disruption of preexisting TRDs and the increase in genomic loops extension outside of TRD domains as described in Fig. 3A. Taken together, we propose that the KSHV 3D genomic structure is designed to maximize the effects of K-Rta complex recruitment and may also facilitate reutilization of active RNAPII complexes.

DISCUSSION

In this report, we have empirically mapped the genomic contacts within the KSHV genome during latency and at an early stage of reactivation. This mapping, combined with bioinformatic tools, has allowed us to uncover TAD-like structures of the KSHV genome during each condition. Using an analysis workflow consisting of HiC-Pro and TADbit, we have constructed a structural model that allows visualization of the overall conformational changes that occur in the viral genome during this time period. With the analyses, similar contact maps were obtained among three PEL cell lines and one laboratory infected cell line (*i*SLK BAC16-Wt). This overall similarity suggests that the prominent viral genome contacts established during latency appear to be conserved among different KSHV infected cell lines and are stable properties within the infected cell population. Although we note that the overall KSHV genomic similarity is

maintained when comparing between BC-1 (KSHV+/EBV+) and BC-3 (KSHV+/EBV-) PEL cell lines (Fig. 1C), the influence of dual infection on viral genomic structure is still an open question and will require additional study.

Previous studies have implicated CTCF sites as being important for several KSHV genomic loops that involve the latency control region and either the K12 or ORF50 locus (31). Inspection of the contact heat maps aligned well with the CTCF/SMC1 recruitment sites at the corners of TRDs, supporting the notion that CTCF/SMC1 plays a major role in defining TRD domains. However, the smaller TRDs also show a lack of CTCF/SMC1 (Fig. 2), possibly reflecting that enriched contacts are not readily visible due to the transient nature of extrusion (49) or that other architectural protein factors could also play a role in structuring latent KSHV genomes. In this respect, KSHV latent genome structures resemble "ordinary domains" as previously defined by Rao et al. (38) to classify contact domains not flanked by CTCF binding sites and formed without involvement of CTCF/cohesin-mediated loop extrusion. As those smaller TADs are separated by transcription units (e.g., gene clusters with genes transcribed in the same direction and having similar kinetics), we speculate that RNA-binding proteins may also play a role in viral genomic structure (50). Although we have highlighted contacts between the ORF50 and K12 loci (13) (Fig. 4) and a potential lncRNA from this region, it should be noted that it is uncertain which gene products originating from promoters in this region might be influenced by genomic looping. This region harbors an origin of lytic replication and the lytic ALT lncRNA running antisense (51). Additional possible candidates are mRNAs encoding the Kaposin locus ORFs as well as a lytic miR-K12-10/12 pri-miRNA (4, 52).

During the shift from latency to lytic replication viral genomes exhibited a loss of local proximal intra-TRD contacts with the widespread onset of inter-TRD contacts (Fig. 3A [a]), while absolute number of KSHV-KSHV genomic contacts were significantly increased (13) (Fig. S1). Seemingly lowered preexisting wiring within TRDs could also be due to relative increased genomic interactions outside of latent TRDs. Consistent with the idea that new interactions exist in tandem with preexisting contacts, widespread eviction of bound CTCF on the KSHV genome is not observed during lytic replication. Rather, CTCF depletion is site-specific with certain regions of the genome exhibiting CTCF loss while binding is preserved at other sites (34). Evidence exists for both dynamic (53–55) and stable (55–58) enhancer-promoter interactions during cellular responses to various stimuli or conditions. In different cell lines or across species, TADs are generally conserved at the megabase scale (14, 39). However, when probed at higher levels of resolution, TADs may merge or be disrupted during changes in gene expression associated with a variety of cellular events such as development (59), lineage commitment (37), reprogramming (60), differentiation (61, 62), senescence (63), and possibly heat shock (64, 65). Together, the current study and our previous report (13), as well as findings from the Lieberman group (31) confirm the existence of both prewired and induced genomic loops and the dynamic nature of KSHV genomic contacts during the viral life cycle.

Insulation scores revealed the strength of borders on the KSHV genome. CTCF, SMC1, and K-Rta frequently bound at the borders, and these sites were decorated by H3K4me3 or H3K27Ac modifications. This observation suggested that K-Rta targets the boundaries established by CTCF and SMC1 with open chromatin structures. By targeting the boundaries, it is likely that K-Rta can recruit K-Rta-bound chromatin remodeling factors (66) to the multiple preassembled genomic regions that frequently tethers stalled RNAPII. In turn, Mediator complex, which is also a part of the K-Rta activation complex (66, 67), may help to establish active genomic hubs for future reactivation in *de novo* infected cells. Further studies will be needed to reveal the potential association of the initial burst of viral transcription following *de novo* infection with the establishment of active latent viral chromatin structure.

The border strength of most viral genomic regions decreased during lytic reactivation. This decrease suggests greater accessibility of a given TRD to interact with other genomic elements, which is accompanied by induction of viral lytic gene transcription.

However, the latency-associated loci remain relatively unchanged. The latency genomic region is, in fact, localized in a small valley, which is well-protected by two strong peaks of CTCF and SMC1 in the KSHV genome (Fig. 1B; genome coordinates 124–130 kbp). The result suggested that the majority of episomes in an infected cell within the given cell populations have similarly maintained CTCF and SMC1 recruitment sites. Accordingly, these highly utilized CTCF/SMC1 binding sites are likely to play very important roles in KSHV latent chromatin in infected cells.

The dynamic nature of the bird cage model is consistent with results obtained using super-resolution imaging of mammalian cell chromatin structures where active histone marks coincided with less compact chromatin and exhibited a higher degree of colocalization with other active marks and RNAP II, while repressive marks coincide with densely packed chromatin and are spatially distant from active RNAP II (68). Wang et al. (69) also noted a decrease in chromatin fiber width when imaging was conducted using nuclei prepared from a quiescent state compared with nuclei undergoing active transcription. These data imply that in the quiescent state, chromatin fibers were more tightly packed together. This was contrasted by chromatin fibers imaged in the actively transcribing state, which appeared to be loosely entangled with each other and to form a relatively thick structure.

We recognize several caveats in our analysis, which is based on calculations assuming linear chromosomes while the KSHV genome is circular, a topology which has implications for interpretation of contact frequencies. Terminal repeats (TR) that occupy approximately one sixth of the KSHV genome (e.g., 28 kb [0.8 kb $\times$ 35 copies]) was also not considered in our analyses due to difficulties in mapping sequence reads. Further studies are therefore needed to confirm where and how a TR interacts with a unique region, which would have significant impact in KSHV reactivation through recruitment of LANA protein complex (47). In addition, we employed a single TAD prediction tool for our analysis; one that allows for 3D modeling. However, it has been documented that TAD prediction algorithms may be very sensitive to data resolution and normalization resulting in calls that vary greatly between tools in terms of TAD number, size, and certain biological properties such as CTCF enrichment around boundaries (70, 71). At the same time, we do have confidence in the 3D structural model of the KSHV genome generated herein and the adequacy of the TADbit approach, based on its assessment conducted by simulations on artificially generated genomes, including a 1-Mb circular chromosome, and subsequent partial verification of the fluorescence *in situ* hybridization imaging (72).

In summary, this study presented 3D KSHV genomic structure models of episomes during latency and early lytic phase of reactivation and revealed the dynamics of genomic interactions by transcription activation. The 3D genomic structures bestow another element to the effectiveness of herpesvirus gene regulation, a system which may provide an opportunity to further study genomic loop regulation through the intersection of viral and host proteins.

MATERIALS AND METHODS

Capture Hi-C. KSHV Capture Hi-C (CHi-C) analysis was performed using a robust *in situ* CHi-C protocol with kitted reagents from Arima Genomics (San Diego, CA) based on well-accepted methods described for *in situ* Hi-C (38, 73), CHI-C (74–76), and as described previously (13). Briefly, cells were cross-linked with 2% formaldehyde, lysed, and genomic DNA digested with a cocktail of 4-cutter restriction endonucleases by incubation for 30 min at 37°C. The 5′ overhangs were then filled in and "marked" with biotin by incorporating biotinylated dATP (biotin-14-dATP) with Klenow fragment of DNA polymerase I (incubation for 45 min at 25°C). Proximally, intramolecular ligation of the blunt-ended fragments was then performed with T4 DNA ligase (incubation for 15 min at 25°C). The formaldehyde cross-links were reversed, and the ligated, chimeric DNA products were purified with Agencourt AMPure XP paramagnetic beads (Beckman Coulter). The DNA was then sheared to an average length of 400 bp using a Covaris E220 Focused-ultrasonicator (Covaris, Inc.) and fragments size-selected with AMPure XP beads to achieve a size distribution of 200–600 bp. The biotin-marked ligation products were then enriched by affinity capture with streptavidin magnetic beads (DynaBeads MyOne Streptavidin C1; Invitrogen, Thermo Fisher Scientific). Subsequently, libraries were prepared from the bound ligation products with the Kapa HyperPrep Kit with Library Amplification Module (Roche) using an on-bead modification to the standard protocol for end repair, dA-tailing, and ligation of Illumina TruSeq sequencing adaptors.

The KSHV CHi-C library was then prepared by target enrichment of the libraries for KSHV genomic content by solution hybridization with a custom-designed KSHV genomic capture probe library (xGen Lockdown Probes; Integrated DNA Technologies, Inc., Coralville, IA) as previously described (13). Briefly, libraries (500 ng) were hybridized with the KSHV genomic capture probe pool (3 pmol) in a mixture containing xGen 1X Hybridization Buffer, Cot-1 (5 μg), and xGen Universal Blocking Oligos for 4 h at 65°C. The hybridized targets were then captured with streptavidin beads (DynaBeads MyOne Streptavidin C1; Thermo Fisher Scientific) by incubation for 45 min at 65°C. Unbound DNA was removed by a series of high-stringency (65°C) and low-stringency (room temperature) washes. The KSHV genome-enriched CHi-C library DNA was eluted, and PCR enrichment (12 cycles) was performed with high-fidelity KAPA HiFi HotStart DNA polymerase (Kapa Biosystems, Inc., Wilmington, MA). Libraries were multiplex sequenced (2 $\times$ 150 bp, paired-end, $\sim$30 million mapped reads/mate pairs per sample) on an Illumina Hiseq 4000 sequencing system (Fig. S1).

Hi-C data preprocessing. Sequence alignment and quality check of reads were performed using HiC-Pro 2.11.1 pipeline (77), each read-end was aligned to the human GRCh37 (hg19) and KSHV (NC_009333.1) reference genomes. Quality reports showed percentage duplicates at less than 15% while >95% di-tags were valid and aligned to restriction fragments (S-Fig. 1). The duplicates were removed and reads mapping only to the KSHV genome were extracted by using Pysam 0.14.1.

Genomic domain analysis. The KSHV genome was analyzed and visualized for frequencies of chimeric genomic reads, and finally modeled for 3D Structure using TADbit (78). The KSHV mapped reads were filtered for only uniquely mapped reads pairs based on the intersection of each read-end. The reads that are self-ligations, dangling-end, error, extra dangling-end, too short, too large, duplicated, and random breaks were filtered out to provide valid reads. The valid reads were stored as matrices and binned with resolution of 500 bp (2 kb for 3D modeling); the bins with more than 1,000 counts and at least 75% of cells with no-zero counts were used in the next steps. Iterative Correction and Eigenvector decomposition (ICE) normalization was used to treat the data with iteration equaling 100. Bins were identified as in compartment A or B by calculating eigenvectors. TADs/TAD borders were called, and insulation score/border strength were calculated using the TADbit computational framework (78) and visualized as contact maps and aligning plots.

KSHV 3D chromosome structure modeling. Matrix modeling potential (MMP) score (72), ranging from 0 to 1, was used to identify if the interaction matrices from the previous step (i.e., iterative modeling with TADbit) have potential for modeling. The higher the MMP scores are, the more likely the 3D model will be accurate. In this study, MMP scores of latency and reactivation models were 0.9541 and 0.9023, respectively. The Monte Carlo optimization method was used to optimize parameters from both models. The parameters included maximal distance associated between two interacting particles, particles attraction, particles repulsion, and contact distance of particles. Sets of models were produced from the possible combinations of those parameters. Contact maps for each set of models were built, then compared with the Hi-C interaction by averages of Spearman correlation coefficients. The models with higher correlation coefficients represented the original data and were chosen to be visualized and plotted by DNA density. The correlations of the latency model and reactivation models were 0.8706 and 0.8782, respectively. Finally, three-dimensional visualization of KSHV molecular modeling were performed with the UCSF Chimera package (48).

Cleavage under targets and release using nuclease (CUT&RUN). Cleavage Under Targets and Release Using Nuclease (CUT&RUN) (79) was performed essentially by following the online protocol established by Dr. Henikoff's lab with a few modifications. Cells were washed with PBS and wash buffer (20 mM HEPES-KOH pH 7.5, 150 mM NaCl, 0.5 mM Spermidine [Sigma, S2626] and proteinase inhibitor [Roche]). After removing the wash buffer, cells were captured on magnetic ConA beads (Polysciences, Warrington, PA, USA) in the presence of $CaCl_2$. beads/cells complexes, were washed 3 times with digitonin wash buffer (0.02% digitonin, 20 mM HEPES-KOH pH 7.5, 150 mM NaCl, 0.5 mM Spermidine and 1$\times$ proteinase inhibitor), aliquoted, and incubated with specific antibodies in 250 μL volume. The antibodies used in this study were: rabbit polyclonal anti-SMC1 (Cell Signaling, #4802S; 1:100), and rabbit monoclonal anti-CTCF (Cell Signaling, clone D31H2, #3418S; 1:100). After incubation, unbound antibody was removed by washing with digitonin wash buffer 3 times. Beads were then incubated with recombinant pAG-MNase, which was purified from *E.coli* (Fig. S4) in 250 μL digitonin wash buffer at 1.0 μg/mL final concentration for 1 h at 4°C with rotation. Unbound pAG-MNase was removed by washing with digitonin wash buffer 3 times. Prechilled 2 mM $CaCl_2$ containing digitonin wash buffer (200 μL) was added to beads and incubated on ice for 30 min. The pAG-MNase digestion was halted by the addition of 200 μL 2$\times$ STOP solution (340 mM NaCl, 20 mM EDTA, 4 mM EGTA, 50 μg/mL RNase A, 50 μg/mL glycogen). The beads were incubated with shaking at 37°C for 10 min in a tube shaker at 500 rpm to release digested DNA fragments from the insoluble nuclear chromatin. The supernatant was collected after centrifugation (16,000 $\times$ *g* for 5 min at 4°C) and placed on a magnetic stand. DNA was extracted using the NucleoSpin kit (TaKaRa Bio, Kusatsu, Shiga, Japan). Sequencing libraries were then prepared from 3 ng of CUT&RUN DNA with the Kapa HyperPrep kit (Roche) according to the manufacturer's standard protocol. Libraries were multiplex sequenced (2 $\times$ 150 bp, paired-end) on an Illumina HiSeq 4000 sequencing system to yield $\sim$15 million mapped reads per sample. When necessary, *E. coli* genomic DNAs contaminating purified pAG-MNase were used to normalize sequence reads, as described previously (79).

Genomic data analysis. FASTQ files for the capture Hi-C experiments were processed through the HiCUP (v0.7.4) pipeline (80) using the KSHV (NC_009333.1) genome. Valid interaction products called by HiCUP were converted into Juicebox (81) input format (.hic file), which stores the normalized and unnormalized contact matrices as a highly compressed binary file, by using a series a scripts provided by HiCUP (hicup2homer) and HOMER (makeTagDirectory and tagDir2hicFile) (82). Juicebox was utilized to facilitate adjustments of resolution and normalization, intensity scaling, zooming, and addition of annotation tracks.

CUT&RUN sequence reads were aligned to the human hg38 reference genome assembly and

reference KSHV genome sequence with Bowtie2 v2.3.5.1 (83) and/or HISAT2 v2.1.0 (84). MACS2 (Model-based Analysis of ChIP-Seq) v2.1.1.1.20160309 was used for detecting peaks (85) following the guidelines in the developer's manual. The following publicly available data sets from previous studies (46, 47) were used to overlay binding sites or histone modification sites: KSHV K-Rta ChIP-seq (GSE123897), H3K27Ac, H3K4me3, and H3K27me3 (GSE163695). Peaks and read alignments were visualized using the Integrated Genome Browser (IGB) (86). Heatmaps and average profile plots were drawn from bed files created by MACS and bam files using the R package, ngsplot v2.63 (87).

Cell culture, bacmid transfection, and selection. TREx-F3-H3-K-Rta BCBL-1 cells (TREx-BCBL-1) cells were maintained and reactivated, as previously described (13). BC-1 and BC-3 cells were maintained in RPMI 1640 supplemented with 15% FBS, 2 mM glutamine, and 1% penicillin-streptomycin. BC-1 and BC-3 cell lines were obtained from the ATCC (Manassas, VA). *i*SLK cells that were infected with BAC16 HA-ORF57 WT virus, were maintained in DMEM supplemented with 10% FBS, 1% penicillin-streptomycin-L-glutamine solution, 1 mg/mL hygromycin B, and 250 μg/mL G418. *i*SLK cells were obtained from Dr. Don Ganem (Novartis Institute for Biomedical Research) and were maintained in DMEM supplemented with 10% FBS, 1% penicillin-streptomycin-L-glutamine solution, 400 μg/mL hygromycin, 250 μg/mL G418, and 10 μg/mL puromycin.

Data availability. The data sets supporting the conclusions of this study are available in the National Center for Biotechnology Information Gene Expression Omnibus (NCBI GEO) repository with the accession code GSE163695.

SUPPLEMENTAL MATERIAL

Supplemental material is available online only.

SUPPLEMENTAL FILE 1, MP4 file, 17.9 MB.

SUPPLEMENTAL FILE 2, MP4 file, 15.2 MB.

SUPPLEMENTAL FILE 3, PDF file, 7.6 MB.

ACKNOWLEDGMENTS

We thank Kenichi Nakajima and Chie Izumiya for technical assistance and other members of the Izumiya lab for discussion and critical reading of the manuscript.

This research was supported by public health grants from National Cancer Institute (CA225266 and CA232845), National Institute of Dental and Craniofacial (DE025985), and National Institute of Allergy and Infectious Diseases (AI147207, AI155515, and AI167663) to Y.I. The Genomics Shared Resource is supported by the UC Davis Comprehensive Cancer Center Support Grant (CCSG) awarded by the National Cancer Institute (NCI P30CA093373).

REFERENCES

1. Bechtel JT, Liang Y, Hvidding J, Ganem D. 2003. Host range of Kaposi's sarcoma-associated herpesvirus in cultured cells. J Virol 77:6474–6481. https://doi.org/10.1128/jvi.77.11.6474-6481.2003.
2. Vieira J, O'Hearn PM. 2004. Use of the red fluorescent protein as a marker of Kaposi's sarcoma-associated herpesvirus lytic gene expression. Virology 325:225–240. https://doi.org/10.1016/j.virol.2004.03.049.
3. Johnson AS, Maronian N, Vieira J. 2005. Activation of Kaposi's sarcoma-associated herpesvirus lytic gene expression during epithelial differentiation. J Virol 79:13769–13777. https://doi.org/10.1128/JVI.79.21.13769-13777.2005.
4. Arias C, Weisburd B, Stern-Ginossar N, Mercier A, Madrid AS, Bellare P, Holdorf M, Weissman JS, Ganem D. 2014. KSHV 2.0: a comprehensive annotation of the Kaposi's sarcoma-associated herpesvirus genome using next-generation sequencing reveals novel genomic and functional features. PLoS Pathog 10:e1003847. https://doi.org/10.1371/journal.ppat.1003847.
5. Bruce AG, Barcy S, DiMaio T, Gan E, Garrigues HJ, Lagunoff M, Rose TM. 2017. Quantitative analysis of the KSHV transcriptome following primary infection of blood and lymphatic endothelial cells. Pathogens 6:11. https://doi.org/10.3390/pathogens6010011.
6. Renne R, Lagunoff M, Zhong W, Ganem D. 1996. The size and conformation of Kaposi's sarcoma-associated herpesvirus (human herpesvirus 8) DNA in infected cells and virions. J Virol 70:8151–8154. https://doi.org/10.1128/JVI.70.11.8151-8154.1996.
7. Lagunoff M, Ganem D. 1997. The structure and coding organization of the genomic termini of Kaposi's sarcoma-associated herpesvirus. Virology 236:147–154. https://doi.org/10.1006/viro.1997.8713.
8. Toth Z, Brulois K, Lee HR, Izumiya Y, Tepper C, Kung HJ, Jung JU. 2013. Biphasic euchromatin-to-heterochromatin transition on the KSHV genome following de novo infection. PLoS Pathog 9:e1003813. https://doi.org/10.1371/journal.ppat.1003813.
9. Toth Z, Brulois K, Jung JU. 2013. The chromatin landscape of Kaposi's sarcoma-associated herpesvirus. Viruses 5:1346–1373. https://doi.org/10.3390/v5051346.
10. Frohlich J, Grundhoff A. 2020. Epigenetic control in Kaposi sarcoma-associated herpesvirus infection and associated disease. Semin Immunopathol 42:143–157. https://doi.org/10.1007/s00281-020-00787-z.
11. Campbell M, Yang WS, Yeh WW, Kao CH, Chang PC. 2020. Epigenetic Regulation of Kaposi's Sarcoma-Associated Herpesvirus Latency. Front Microbiol 11:850. https://doi.org/10.3389/fmicb.2020.00850.
12. Chang PC, Fitzgerald LD, Hsia DA, Izumiya Y, Wu CY, Hsieh WP, Lin SF, Campbell M, Lam KS, Luciw PA, Tepper CG, Kung HJ. 2011. Histone demethylase JMJD2A regulates Kaposi's sarcoma-associated herpesvirus replication and is targeted by a viral transcriptional factor. J Virol 85:3283–3293. https://doi.org/10.1128/JVI.02485-10.
13. Campbell M, Watanabe T, Nakano K, Davis RR, Lyu Y, Tepper CG, Durbin-Johnson B, Fujimuro M, Izumiya Y. 2018. KSHV episomes reveal dynamic chromatin loop formation with domain-specific gene regulation. Nat Commun 9:49. https://doi.org/10.1038/s41467-017-02089-9.
14. Dixon JR, Selvaraj S, Yue F, Kim A, Li Y, Shen Y, Hu M, Liu JS, Ren B. 2012. Topological domains in mammalian genomes identified by analysis of chromatin interactions. Nature 485:376–380. https://doi.org/10.1038/nature11082.
15. Nora EP, Lajoie BR, Schulz EG, Giorgetti L, Okamoto I, Servant N, Piolot T, van Berkum NL, Meisig J, Sedat J, Gribnau J, Barillot E, Bluthgen N, Dekker J, Heard E. 2012. Spatial partitioning of the regulatory landscape of the X-inactivation centre. Nature 485:381–385. https://doi.org/10.1038/nature11049.
16. Dekker J, Mirny L. 2016. The 3D genome as moderator of chromosomal communication. Cell 164:1110–1121. https://doi.org/10.1016/j.cell.2016.02.007.

17. Sexton T, Yaffe E, Kenigsberg E, Bantignies F, Leblanc B, Hoichman M, Parrinello H, Tanay A, Cavalli G. 2012. Three-dimensional folding and functional organization principles of the Drosophila genome. Cell 148:458–472. https://doi.org/10.1016/j.cell.2012.01.010.
18. Lieberman-Aiden E, van Berkum NL, Williams L, Imakaev M, Ragoczy T, Telling A, Amit I, Lajoie BR, Sabo PJ, Dorschner MO, Sandstrom R, Bernstein B, Bender MA, Groudine M, Gnirke A, Stamatoyannopoulos J, Mirny LA, Lander ES, Dekker J. 2009. Comprehensive mapping of long-range interactions reveals folding principles of the human genome. Science 326:289–293. https://doi.org/10.1126/science.1181369.
19. Dostie J, Richmond TA, Arnaout RA, Selzer RR, Lee WL, Honan TA, Rubio ED, Krumm A, Lamb J, Nusbaum C, Green RD, Dekker J. 2006. Chromosome Conformation Capture Carbon Copy (5C): a massively parallel solution for mapping interactions between genomic elements. Genome Res 16:1299–1309. https://doi.org/10.1101/gr.5571506.
20. Gomez-Marin C, Tena JJ, Acemel RD, Lopez-Mayorga M, Naranjo S, de la Calle-Mustienes E, Maeso I, Beccari L, Aneas I, Vielmas E, Bovolenta P, Nobrega MA, Carvajal J, Gomez-Skarmeta JL. 2015. Evolutionary comparison reveals that diverging CTCF sites are signatures of ancestral topological associating domains borders. Proc Natl Acad Sci U S A 112:7542–7547. https://doi.org/10.1073/pnas.1505463112.
21. Crane E, Bian Q, McCord RP, Lajoie BR, Wheeler BS, Ralston EJ, Uzawa S, Dekker J, Meyer BJ. 2015. Condensin-driven remodelling of X chromosome topology during dosage compensation. Nature 523:240–244. https://doi.org/10.1038/nature14450.
22. Hsieh TH, Weiner A, Lajoie B, Dekker J, Friedman N, Rando OJ. 2015. Mapping nucleosome resolution chromosome folding in yeast by Micro-C. Cell 162:108–119. https://doi.org/10.1016/j.cell.2015.05.048.
23. Mizuguchi T, Fudenberg G, Mehta S, Belton JM, Taneja N, Folco HD, FitzGerald P, Dekker J, Mirny L, Barrowman J, Grewal SIS. 2014. Cohesin-dependent globules and heterochromatin shape 3D genome architecture in S. pombe. Nature 516:432–435. https://doi.org/10.1038/nature13833.
24. Le TB, Imakaev MV, Mirny LA, Laub MT. 2013. High-resolution mapping of the spatial organization of a bacterial chromosome. Science 342:731–734. https://doi.org/10.1126/science.1242059.
25. Marbouty M, Le Gall A, Cattoni DI, Cournac A, Koh A, Fiche JB, Mozziconacci J, Murray H, Koszul R, Nollmann M. 2015. Condensin- and replication-mediated bacterial chromosome folding and origin condensation revealed by Hi-C and super-resolution imaging. Mol Cell 59:588–602. https://doi.org/10.1016/j.molcel.2015.07.020.
26. Wang X, Le TB, Lajoie BR, Dekker J, Laub MT, Rudner DZ. 2015. Condensin promotes the juxtaposition of DNA flanking its loading site in Bacillus subtilis. Genes Dev 29:1661–1675. https://doi.org/10.1101/gad.265876.115.
27. Rowley MJ, Corces VG. 2016. The three-dimensional genome: principles and roles of long-distance interactions. Curr Opin Cell Biol 40:8–14. https://doi.org/10.1016/j.ceb.2016.01.009.
28. Stedman W, Kang H, Lin S, Kissil JL, Bartolomei MS, Lieberman PM. 2008. Cohesins localize with CTCF at the KSHV latency control region and at cellular c-myc and H19/Igf2 insulators. EMBO J 27:654–666. https://doi.org/10.1038/emboj.2008.1.
29. Kang H, Lieberman PM. 2009. Cell cycle control of Kaposi's sarcoma-associated herpesvirus latency transcription by CTCF-cohesin interactions. J Virol 83:6199–6210. https://doi.org/10.1128/JVI.00052-09.
30. Kang H, Lieberman PM. 2011. Mechanism of glycyrrhizic acid inhibition of Kaposi's sarcoma-associated herpesvirus: disruption of CTCF-cohesin-mediated RNA polymerase II pausing and sister chromatid cohesion. J Virol 85:11159–11169. https://doi.org/10.1128/JVI.00720-11.
31. Kang H, Wiedmer A, Yuan Y, Robertson E, Lieberman PM. 2011. Coordination of KSHV latent and lytic gene control by CTCF-cohesin mediated chromosome conformation. PLoS Pathog 7:e1002140. https://doi.org/10.1371/journal.ppat.1002140.
32. Chen HS, Wikramasinghe P, Showe L, Lieberman PM. 2012. Cohesins repress Kaposi's sarcoma-associated herpesvirus immediate early gene transcription during latency. J Virol 86:9454–9464. https://doi.org/10.1128/JVI.00787-12.
33. Kang H, Cho H, Sung GH, Lieberman PM. 2013. CTCF regulates Kaposi's sarcoma-associated herpesvirus latency transcription by nucleosome displacement and RNA polymerase programming. J Virol 87:1789–1799. https://doi.org/10.1128/JVI.02283-12.
34. Li DJ, Verma D, Mosbruger T, Swaminathan S. 2014. CTCF and Rad21 act as host cell restriction factors for Kaposi's sarcoma-associated herpesvirus (KSHV) lytic replication by modulating viral gene transcription. PLoS Pathog 10:e1003880. https://doi.org/10.1371/journal.ppat.1003880.
35. Toth Z, Smindak RJ, Papp B. 2017. Inhibition of the lytic cycle of Kaposi's sarcoma-associated herpesvirus by cohesin factors following de novo infection. Virology 512:25–33. https://doi.org/10.1016/j.virol.2017.09.001.
36. Li D, Mosbruger T, Verma D, Swaminathan S. 2020. Complex interactions between Cohesin and CTCF in regulation of Kaposi's sarcoma-associated herpesvirus lytic transcription. J Virol 94. https://doi.org/10.1128/JVI.01279-19.
37. Phillips-Cremins JE, Sauria ME, Sanyal A, Gerasimova TI, Lajoie BR, Bell JS, Ong CT, Hookway TA, Guo C, Sun Y, Bland MJ, Wagstaff W, Dalton S, McDevitt TC, Sen R, Dekker J, Taylor J, Corces VG. 2013. Architectural protein subclasses shape 3D organization of genomes during lineage commitment. Cell 153:1281–1295. https://doi.org/10.1016/j.cell.2013.04.053.
38. Rao SS, Huntley MH, Durand NC, Stamenova EK, Bochkov ID, Robinson JT, Sanborn AL, Machol I, Omer AD, Lander ES, Aiden EL. 2014. A 3D map of the human genome at kilobase resolution reveals principles of chromatin looping. Cell 159:1665–1680. https://doi.org/10.1016/j.cell.2014.11.021.
39. Vietri Rudan M, Barrington C, Henderson S, Ernst C, Odom DT, Tanay A, Hadjur S. 2015. Comparative Hi-C reveals that CTCF underlies evolution of chromosomal domain architecture. Cell Rep 10:1297–1309. https://doi.org/10.1016/j.celrep.2015.02.004.
40. Toth Z, Maglinte DT, Lee SH, Lee HR, Wong LY, Brulois KF, Lee S, Buckley JD, Laird PW, Marquez VE, Jung JU. 2010. Epigenetic analysis of KSHV latent and lytic genomes. PLoS Pathog 6:e1001013. https://doi.org/10.1371/journal.ppat.1001013.
41. Gunther T, Grundhoff A. 2010. The epigenetic landscape of latent Kaposi sarcoma-associated herpesvirus genomes. PLoS Pathog 6:e1000935. https://doi.org/10.1371/journal.ppat.1000935.
42. Kim KY, Huerta SB, Izumiya C, Wang DH, Martinez A, Shevchenko B, Kung HJ, Campbell M, Izumiya Y. 2013. Kaposi's sarcoma-associated herpesvirus (KSHV) latency-associated nuclear antigen regulates the KSHV epigenome by association with the histone demethylase KDM3A. J Virol 87:6782–6793. https://doi.org/10.1128/JVI.00011-13.
43. Hu J, Yang Y, Turner PC, Jain V, McIntyre LM, Renne R. 2014. LANA binds to multiple active viral and cellular promoters and associates with the H3K4methyltransferase hSET1 complex. PLoS Pathog 10:e1004240. https://doi.org/10.1371/journal.ppat.1004240.
44. Davis RR, Campbell M, Izumiya Y, Tepper CG. 2020. Capture Hi-C: characterization of chromatin contacts, p 429–444. *In* Tollefsbol T (ed), Translational epigenetics. Epigenetics methods, vol 18. Academic Press, New York, NY.
45. Gavrilov A, Eivazova E, Priozhkova I, Lipinski M, Razin S, Vassetzky Y. 2009. Chromosome conformation capture (from 3C to 5C) and its ChIP-based modification. Methods Mol Biol 567:171–188. https://doi.org/10.1007/978-1-60327-414-2_12.
46. Papp B, Motlagh N, Smindak RJ, Jin Jang S, Sharma A, Alonso JD, Toth Z. 2019. Genome-wide identification of direct RTA targets reveals key host factors for Kaposi's sarcoma-associated herpesvirus lytic reactivation. J Virol 93. https://doi.org/10.1128/JVI.01978-18.
47. Kumar A, Lyu Y, Yanagihashi Y, Chantarasrivong C, Majerciak V, Salemi M, Wang KH, Inagaki T, Chuang F, Davis RR, Tepper CG, Nakano K, Izumiya C, Shimoda M, Nakajima KI, Merleev A, Zheng ZM, Campbell M, Izumiya Y. 2022. KSHV episome tethering sites on host chromosomes and regulation of latency-lytic switch by CHD4. Cell Rep 39:110788. In press. https://doi.org/10.1016/j.celrep.2022.110788.
48. Pettersen EF, Goddard TD, Huang CC, Couch GS, Greenblatt DM, Meng EC, Ferrin TE. 2004. UCSF Chimera–a visualization system for exploratory research and analysis. J Comput Chem 25:1605–1612. https://doi.org/10.1002/jcc.20084.
49. Sanborn AL, Rao SS, Huang SC, Durand NC, Huntley MH, Jewett AI, Bochkov ID, Chinnappan D, Cutkosky A, Li J, Geeting KP, Gnirke A, Melnikov A, McKenna D, Stamenova EK, Lander ES, Aiden EL. 2015. Chromatin extrusion explains key features of loop and domain formation in wild-type and engineered genomes. Proc Natl Acad Sci U S A 112:E6456–6465. https://doi.org/10.1073/pnas.1518552112.
50. Bertero A, Fields PA, Ramani V, Bonora G, Yardimci GG, Reinecke H, Pabon L, Noble WS, Shendure J, Murry CE. 2019. Dynamics of genome reorganization during human cardiogenesis reveal an RBM20-dependent splicing factory. Nat Commun 10:1538. https://doi.org/10.1038/s41467-019-09483-5.
51. Schifano JM, Corcoran K, Kelkar H, Dittmer DP. 2017. Expression of the antisense-to-latency transcript long noncoding RNA in Kaposi's sarcoma-associated herpesvirus. J Virol 91. https://doi.org/10.1128/JVI.01698-16.
52. Qin J, Li W, Gao SJ, Lu C. 2017. KSHV microRNAs: tricks of the devil. Trends Microbiol 25:648–661. https://doi.org/10.1016/j.tim.2017.02.002.

53. Tolhuis B, Palstra RJ, Splinter E, Grosveld F, de Laat W. 2002. Looping and interaction between hypersensitive sites in the active beta-globin locus. Mol Cell 10:1453–1465. https://doi.org/10.1016/s1097-2765(02)00781-5.
54. Li L, Zhang JA, Dose M, Kueh HY, Mosadeghi R, Gounari F, Rothenberg EV. 2013. A far downstream enhancer for murine Bcl11b controls its T-cell specific expression. Blood 122:902–911. https://doi.org/10.1182/blood-2012-08-447839.
55. Rubin AJ, Barajas BC, Furlan-Magaril M, Lopez-Pajares V, Mumbach MR, Howard I, Kim DS, Boxer LD, Cairns J, Spivakov M, Wingett SW, Shi M, Zhao Z, Greenleaf WJ, Kundaje A, Snyder M, Chang HY, Fraser P, Khavari PA. 2017. Lineage-specific dynamic and pre-established enhancer-promoter contacts cooperate in terminal differentiation. Nat Genet 49:1522–1528. https://doi.org/10.1038/ng.3935.
56. Jin F, Li Y, Dixon JR, Selvaraj S, Ye Z, Lee AY, Yen CA, Schmitt AD, Espinoza CA, Ren B. 2013. A high-resolution map of the three-dimensional chromatin interactome in human cells. Nature 503:290–294. https://doi.org/10.1038/nature12644.
57. Ghavi-Helm Y, Klein FA, Pakozdi T, Ciglar L, Noordermeer D, Huber W, Furlong EE. 2014. Enhancer loops appear stable during development and are associated with paused polymerase. Nature 512:96–100. https://doi.org/10.1038/nature13417.
58. Platt JL, Salama R, Smythies J, Choudhry H, Davies JO, Hughes JR, Ratcliffe PJ, Mole DR. 2016. Capture-C reveals preformed chromatin interactions between HIF-binding sites and distant promoters. EMBO Rep 17:1410–1421. https://doi.org/10.15252/embr.201642198.
59. Bonev B, Mendelson Cohen N, Szabo Q, Fritsch L, Papadopoulos GL, Lubling Y, Xu X, Lv X, Hugnot JP, Tanay A, Cavalli G. 2017. Multiscale 3D genome rewiring during mouse neural development. Cell 171:557–572.e524. https://doi.org/10.1016/j.cell.2017.09.043.
60. Stadhouders R, Vidal E, Serra F, Di Stefano B, Le Dily F, Quilez J, Gomez A, Collombet S, Berenguer C, Cuartero Y, Hecht J, Filion GJ, Beato M, Marti-Renom MA, Graf T. 2018. Transcription factors orchestrate dynamic interplay between genome topology and gene regulation during cell reprogramming. Nat Genet 50:238–249. https://doi.org/10.1038/s41588-017-0030-7.
61. Dixon JR, Jung I, Selvaraj S, Shen Y, Antosiewicz-Bourget JE, Lee AY, Ye Z, Kim A, Rajagopal N, Xie W, Diao Y, Liang J, Zhao H, Lobanenkov VV, Ecker JR, Thomson JA, Ren B. 2015. Chromatin architecture reorganization during stem cell differentiation. Nature 518:331–336. https://doi.org/10.1038/nature14222.
62. Siersbæk R, Madsen JGS, Javierre BM, Nielsen R, Bagge EK, Cairns J, Wingett SW, Traynor S, Spivakov M, Fraser P, Mandrup S. 2017. Dynamic rewiring of promoter-anchored chromatin loops during adipocyte differentiation. Mol Cell 66:420–435 e425. https://doi.org/10.1016/j.molcel.2017.04.010.
63. Criscione SW, De Cecco M, Siranosian B, Zhang Y, Kreiling JA, Sedivy JM, Neretti N. 2016. Reorganization of chromosome architecture in replicative cellular senescence. Sci Adv 2:e1500882. https://doi.org/10.1126/sciadv.1500882.
64. Li L, Lyu X, Hou C, Takenaka N, Nguyen HQ, Ong CT, Cubenas-Potts C, Hu M, Lei EP, Bosco G, Qin ZS, Corces VG. 2015. Widespread rearrangement of 3D chromatin organization underlies polycomb-mediated stress-induced silencing. Mol Cell 58:216–231. https://doi.org/10.1016/j.molcel.2015.02.023.
65. Ray J, Munn PR, Vihervaara A, Lewis JJ, Ozer A, Danko CG, Lis JT. 2019. Chromatin conformation remains stable upon extensive transcriptional changes driven by heat shock. Proc Natl Acad Sci U S A 116:19431–19439. https://doi.org/10.1073/pnas.1901244116.
66. Shimoda M, Lyu Y, Wang KH, Kumar A, Miura H, Meckler JF, Davis RR, Chantarasrivong C, Izumiya C, Tepper CG, Nakajima KI, Tuscano J, Barisone G, Izumiya Y. 2021. KSHV transactivator-derived small peptide traps coactivators to attenuate MYC and inhibits leukemia and lymphoma cell growth. Commun Biol 4:1330. https://doi.org/10.1038/s42003-021-02853-0.
67. Gwack Y, Baek HJ, Nakamura H, Lee SH, Meisterernst M, Roeder RG, Jung JU. 2003. Principal role of TRAP/mediator and SWI/SNF complexes in Kaposi's sarcoma-associated herpesvirus RTA-mediated lytic reactivation. Mol Cell Biol 23:2055–2067. https://doi.org/10.1128/MCB.23.6.2055-2067.2003.
68. Xu J, Ma H, Jin J, Uttam S, Fu R, Huang Y, Liu Y. 2018. Super-resolution imaging of higher-order chromatin structures at different epigenomic states in single mammalian cells. Cell Rep 24:873–882. https://doi.org/10.1016/j.celrep.2018.06.085.
69. Wang Y, Maharana S, Wang MD, Shivashankar GV. 2014. Super-resolution microscopy reveals decondensed chromatin structure at transcription sites. Sci Rep 4:4477. https://doi.org/10.1038/srep04477.
70. Dali R, Blanchette M. 2017. A critical assessment of topologically associating domain prediction tools. Nucleic Acids Res 45:2994–3005. https://doi.org/10.1093/nar/gkx145.
71. Zufferey M, Tavernari D, Oricchio E, Ciriello G. 2018. Comparison of computational methods for the identification of topologically associating domains. Genome Biol 19:217. https://doi.org/10.1186/s13059-018-1596-9.
72. Trussart M, Serra F, Bau D, Junier I, Serrano L, Marti-Renom MA. 2015. Assessing the limits of restraint-based 3D modeling of genomes and genomic domains. Nucleic Acids Res 43:3465–3477. https://doi.org/10.1093/nar/gkv221.
73. Belaghzal H, Dekker J, Gibcus JH. 2017. Hi-C 2.0: An optimized Hi-C procedure for high-resolution genome-wide mapping of chromosome conformation. Methods 123:56–65. https://doi.org/10.1016/j.ymeth.2017.04.004.
74. Schmitt AD, Hu M, Ren B. 2016. Genome-wide mapping and analysis of chromosome architecture. Nat Rev Mol Cell Biol 17:743–755. https://doi.org/10.1038/nrm.2016.104.
75. Schoenfelder S, Javierre BM, Furlan-Magaril M, Wingett SW, Fraser P. 2018. Promoter capture Hi-C: high-resolution, genome-wide profiling of promoter interactions. J Vis Exp https://doi.org/10.3791/57320.
76. Jung I, Schmitt A, Diao Y, Lee AJ, Liu T, Yang D, Tan C, Eom J, Chan M, Chee S, Chiang Z, Kim C, Masliah E, Barr CL, Li B, Kuan S, Kim D, Ren B. 2019. A compendium of promoter-centered long-range chromatin interactions in the human genome. Nat Genet 51:1442–1449. https://doi.org/10.1038/s41588-019-0494-8.
77. Servant N, Varoquaux N, Lajoie BR, Viara E, Chen CJ, Vert JP, Heard E, Dekker J, Barillot E. 2015. HiC-Pro: an optimized and flexible pipeline for Hi-C data processing. Genome Biol 16:259. https://doi.org/10.1186/s13059-015-0831-x.
78. Serra F, Bau D, Goodstadt M, Castillo D, Filion GJ, Marti-Renom MA. 2017. Automatic analysis and 3D-modelling of Hi-C data using TADbit reveals structural features of the fly chromatin colors. PLoS Comput Biol 13:e1005665. https://doi.org/10.1371/journal.pcbi.1005665.
79. Skene PJ, Henikoff S. 2017. An efficient targeted nuclease strategy for high-resolution mapping of DNA binding sites. Elife 6. https://doi.org/10.7554/eLife.21856.
80. Wingett S, Ewels P, Furlan-Magaril M, Nagano T, Schoenfelder S, Fraser P, Andrews S. 2015. HiCUP: pipeline for mapping and processing Hi-C data. F1000Res 4:1310. https://doi.org/10.12688/f1000research.7334.1.
81. Durand NC, Robinson JT, Shamim MS, Machol I, Mesirov JP, Lander ES, Aiden EL. 2016. Juicebox provides a visualization system for Hi-C contact maps with unlimited zoom. Cell Syst 3:99–101. https://doi.org/10.1016/j.cels.2015.07.012.
82. Heinz S, Benner C, Spann N, Bertolino E, Lin YC, Laslo P, Cheng JX, Murre C, Singh H, Glass CK. 2010. Simple combinations of lineage-determining transcription factors prime cis-regulatory elements required for macrophage and B cell identities. Mol Cell 38:576–589. https://doi.org/10.1016/j.molcel.2010.05.004.
83. Langmead B, Salzberg SL. 2012. Fast gapped-read alignment with Bowtie 2. Nat Methods 9:357–359. https://doi.org/10.1038/nmeth.1923.
84. Kim D, Paggi JM, Park C, Bennett C, Salzberg SL. 2019. Graph-based genome alignment and genotyping with HISAT2 and HISAT-genotype. Nat Biotechnol 37:907–915. https://doi.org/10.1038/s41587-019-0201-4.
85. Zhang Y, Liu T, Meyer CA, Eeckhoute J, Johnson DS, Bernstein BE, Nusbaum C, Myers RM, Brown M, Li W, Liu XS. 2008. Model-based analysis of ChIP-Seq (MACS). Genome Biol 9:R137. https://doi.org/10.1186/gb-2008-9-9-r137.
86. Freese NH, Norris DC, Loraine AE. 2016. Integrated genome browser: visual analytics platform for genomics. Bioinformatics 32:2089–2095. https://doi.org/10.1093/bioinformatics/btw069.
87. Shen L, Shao N, Liu X, Nestler E. 2014. ngs.plot: Quick mining and visualization of next-generation sequencing data by integrating genomic databases. BMC Genomics 15:284. https://doi.org/10.1186/1471-2164-15-284.